JOURNAL OF MECHANICS OF CONTINUA AND
MATHEMATICAL SCIENCES
www.journalimcms.org

ISSN (Online) : 2454 -7190 Vol.-21, No.-04, April (2026) pp 87-111 ISSN (Print) 0973-8975

A SINE - COSINE WAVELET OPERATIONAL MATRIX SOLUTION OF A POROELASTIC SQUEEZE FILM LUBRICATION MODEL WITH APPLICATION TO HIP JOINT BIO LUBRICATIONS

S. C. Shiralashetti[1], **Vatsala N. T.**[2]

[1,2] Department of Mathematics, Karnatak University, Dharwad-580003,
Karnataka, India.

Email: [1]scshiralashetti@kud.ac.in, [2]vatsalavatsala0189@gmail.com

Corresponding Author: **S. C. Shiralashetti**

https://doi.org/10.26782/jmcms.2026.04.00005

(Received: January 17, 2026; Revised: April 02, 2026; Accepted : April 16, 2026)

Abstract

The squeeze film behaviour of poroelastic bearings with rough surfaces and couple stress fluids is studied using a simplified model in which the action of the couple stress synovial fluid in lubricating the hip joint is examined. The articular cartilage. The layer is modelled as a biphasic poroelastic matrix material. A modified average Reynolds equation is derived, which accounts for the couple stress effects, random surface roughness, and the elastic nature of the cartilage-bearing surface. Two types of one-dimensional random roughness patterns, longitudinal roughness and transverse roughness, are presented using Christensen's stochastic theory. By using a domain transformation, the reduced governing equations can be mapped onto the unit square and solved numerically using the sine-cosine wavelet operational matrix of integration method. Uniqueness, uniform convergence, convergence of the partial sums to the exact function, and commutation of the integration and limit operations are guaranteed by proving some properties of the wavelet approximation. The numerical results indicate that, although couple stresses can improve the performance of the joint as a whole, the effect on the squeeze film performance of surface roughness must be considered, depending on the patterns of surface roughness. The wavelet-based method proposed in this paper is accurate and efficient.

Keywords: Sine cosine wavelet operational matrix of integration (SCWOMI), Poroelastic Squeeze film, longitudinal roughness, transverse roughness, Finite difference method.

I. Introduction

Smooth articulation under high physiological loads is possible because of load-bearing biomechanical systems known as synovial joints [XVII]. These joints consist of closely fitting surfaces that are separated by synovial fluid and covered by articular cartilage. These components work together to provide low wear, low friction, and effective shock absorption during movement [XIII]. The hip joint, which is one of the synovial joints, plays a key role in human movement. It can handle dynamic loads that are several times the body weight while allowing for a range of motions [XX].

The poroelastic structure and mechanical properties of articular cartilage, a porous, fluid-filled, and flexible tissue, are closely connected to its tribological performance [XXVI, XXVII]. Traditional Newtonian lubrication theory cannot fully explain the non-Newtonian behaviour of synovial fluid, which includes long-chain hyaluronic acid molecules. Couple stress fluid theory has been widely used as an effective modelling approach for synovial lubrication to capture these microstructural effects [I, XIV, III]. The properties of squeeze film are primarily influenced by the surface roughness of articular cartilage, along with poroelasticity and non-Newtonian fluid behaviour. Research shows that cartilage surfaces are naturally rough with random distributions [XXIII]. Christensen's stochastic theory has been effectively used in various bearing designs and provides a mathematically sound way to include roughness effects in hydrodynamic lubrication models [XXX, IV]. Surface roughness can significantly alter pressure distribution and load-carrying ability in squeeze film conditions, where the film thickness approaches the roughness amplitudes [XVI].

Squeeze film lubrication is controlled by nonlinear two-dimensional partial differential equations [XXIX, V, XXI]. These equations are affected by poroelastic deformation, coupled stress fluid effects, and surface roughness [XVIII, XXVII, XV, X]. Since there are usually no analytical solutions for these problems, numerical methods are necessary [XXXII]. Previous studies have employed traditional techniques like finite difference and finite element methods [VII, VIII]. However, these methods often require fine discretisation and can result in higher processing costs, especially for problems defined on finite domains.

Wavelet-based numerical techniques have become strong alternatives due to their good approximation qualities, orthogonality, and ability to handle multiple resolutions. Sine-cosine wavelets are especially suitable for problems defined on limited intervals because of their simple structure and clear analytical form [IX]. The operational matrix of integration for wavelets allows for the conversion of differential equations into systems of algebraic equations, making numerical implementation easier [XII, XXIV]. However, there are still a few applications of sine-cosine wavelet operational matrix techniques to two-dimensional lubrication problems involving Couple stress fluids and poroelastic materials [VI, XXII]. Additionally, there is a lack of thorough theoretical study regarding the validity, uniform convergence, and uniqueness of term-wise operations in two-dimensional settings. To study the squeeze film lubrication of rough poroelastic partial journal bearings using Couple stress fluids, particularly for hip joint lubrication, this work develops a sine-cosine wavelet operational matrix of integration approach [XIX, II, XXV]. A wavelet-based approximation is effectively achieved by mapping the governing equations onto a unit square. with a suitable domain transformation. The uniqueness of the two-dimensional wavelet expansion, uniform convergence of the approximation, convergence of partial sums, and the ability to interchange limits and integration are some of the theoretical results established to ensure the reliability of the numerical scheme [XXXI, XI].

The main novelties and contributions of this work can be summarised as follows:

Wavelet Based Numerical Framework: A sine-cosine wavelet operational matrix for integration is developed and used to solve the two-dimensional modified Reynolds equation.

Domain Transformation Strategy: A suitable domain transformation is used to map the physical lubrication domain onto a unit square. This allows for the direct and efficient implementation of the sine-cosine wavelet basis.

Novel Theoretical Findings: For the two-dimensional sine-cosine wavelet approximation, several new mathematical conclusions are established, such as the wavelet expansion's uniqueness, uniform convergence of the approximation, and uniform partial sum convergence. These findings give the proposed operational matrix approach a strong theoretical foundation.

Use in Hip Joint Lubrication: The proposed approach is used to study how surface roughness patterns, poroelastic parameters, and couple stress fluid properties impact squeeze film lubrication performance. This offers new insights into hip joint tribology.

Efficiency of Computation: Compared to traditional numerical methods, the wavelet-based technique shows greater computing efficiency by reaching correct solutions with basis functions.

II. Mathematical Model

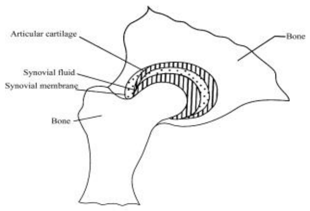

Fig. 1: A diagram of the Hip Joint

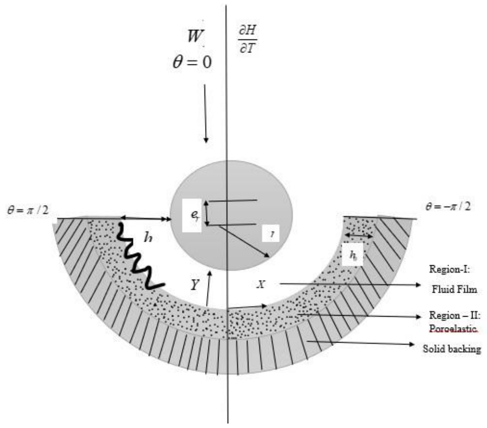

Fig. 2: The geometric configuration of the simplified hip joint mode

Fig.1. shows the structure of the human hip. Fig. 2 displays a simplified hip joint lubrication system. This system acts as a finite, partly rough poroelastic journal bearing that works under squeeze film conditions without any rotational movement. In the illustration, a journal with a radius r moves toward a compliant poroelastic surface with a thickness of h_0 at a specific angle θ. It is driven by a normal approach speed dH / dT. Stokes pair stress theory explains how the lubricant layer behaves as an incompressible non-Newtonian fluid. The thickness of the fluid film is treated as a

random variable, consisting of two different parts to account for the effects of imperfections on the cartilage surface.

$$h = H + H_s(\theta, Z, \varsigma) \tag{1}$$

Here, the ideal smooth part of the lubricant film profile is shown by the formula $H = c - e_r \cos\theta$. The additional contribution $H_s(\theta, Z, \varsigma)$ is a zero-mean random variable. It accounts for changes caused by tiny surface unevenness compared to the reference surface. A specific instance of the roughness pattern is described by the parameter ς. The eccentricity ratio is defined as $E = e_r / c$. In this formulation, c represents the radial clearance of the bearing. The angular coordinate along the circumference is given by $\theta = (X / r)$, where r is the journal radius.

Basic Equations

Region – I:

The equations that govern mass conservation and momentum balance for a fluid showing pair stress effects can be expressed as follows using the Stokes micro continuum framework [XXIII].

$$\nabla \vec{v} = 0$$

$$\frac{\sigma D\vec{v}}{DT} = -\nabla P + \mu_v \nabla^2 \vec{v} - \eta_c \nabla^4 \vec{v} \tag{2}$$

The lubricant's velocity field is represented by $\vec{v}$, fluid density by σ, hydrodynamic pressure by P, dynamic viscosity by μ_v, and the material parameter related to the coupling stress behaviour by η_c. In this research, the lubricant can be treated as a Stokes-type pair stress fluid because it is thought to contain polymeric additives with long molecular chains. The effects of external body forces and body partners are ignored, and the lubricating layer is considered thin enough. When the equations that regulate lubricant flow are represented in a Cartesian coordinate system, they become simpler under these assumptions.

$$\frac{\partial U}{\partial X} + \frac{\partial V}{\partial Y} + \frac{\partial W}{\partial Z} = 0 \tag{3}$$

$$\mu_v \frac{\partial^2 U}{\partial Y^2} - \eta_c \frac{\partial^4 U}{\partial Y^4} = \frac{\partial P}{\partial X} \tag{4}$$

$$\frac{\partial P}{\partial Y} = 0 \tag{5}$$

$$\mu_v \frac{\partial^2 W}{\partial Y^2} - \eta_c \frac{\partial^4 W}{\partial Y^4} = \frac{\partial P}{\partial Z} \tag{6}$$

The fluid velocity components along the U, V and W axes are represented by X, Y and Z, respectively.

Region – II:

A changed version of the model introduced by Torzilli and Mow [XXVII] is used to set up the quasi-static, coupled equations that control the movement of the deformable cartilage solid structure and the interstitial fluid in its pore spaces.

$$div\,\rho_s - \frac{1}{K^*}\left(\frac{d\vec{W}}{dT} - \vec{v}^*\right) = 0 \tag{7a}$$

$$div\,\rho_f + \frac{1}{K^*}\left(\frac{d\vec{W}}{dT} - \vec{v}^*\right) = 0 \tag{7b}$$

In this expression, ρ_s and ρ_f represent the effective stress tensors linked to the fluid phase and the solid cartilage framework, respectively. The displacement of the cartilage matrix is described by the vector $\vec{\omega}$, the interstitial fluid velocity is given by $\vec{v}^*$, and the hydraulic permeability of the cartilaginous tissue is denoted by K^*. The momentum balance conditions for the solid structure and the synovial fluid filling the pore gaps are outlined in equations (7a) and (7b). The coupling terms in these equations account for the viscous drag caused by the relative motion between the solid matrix and the pore fluid. Both stages are treated as incompressible.

Since the drag coefficient k is still quite low, around 10−15 Nsm^{-4}, it makes sense to ignore inertial effects. Even without any external loading, for low-speed deformation processes, there is a relationship between the drag coefficient. k and the tissue permeability K^* [XV].

$$K^* = \frac{1}{(1+\beta)^2 k} \tag{8}$$

In this case, β represents the ratio of the solid fraction to the tissue's pore volume. The resulting equations can be shown in their modified form by applying the assumptions mentioned earlier to the general relationships that govern each phase.

$$\rho_s = P^* I + B\,tr\,e_{rs} I + M e_{rs} \tag{9a}$$

$$\rho_f = -P^* I + D\,tr\,e_{rs} I \tag{9b}$$

The constitutive relations given in equations (9a) and (9b), together with the governing equations (7a) and (7b), establish the coupling between the pore pressure. P^*, strain tensor e_{rs}, and fluid velocity $\vec{v}^*$. In this formulation, the pore pressure influences the deformation of the solid matrix through volumetric strain, while the deformation affects fluid flow via permeability. K^* and drag interactions. Hence, all dependent variables are interrelated, ensuring that the poroelastic model forms a closed system. Taking the divergence of the resulting expression leads to the following Laplace-type equation.

$$\nabla^2 tr(e_{rs}) = 0 \tag{10}$$

In this case, $tr(e_{rs})$ shows the volumetric strain, which is the cartilage's dilatation. Based on the idea presented by Hori and Mockros [X], the following expression connects the bulk modulus B_m to the hydrostatic pressure P^*.

$$tr\,(e_{rs}) = e_{r0} + \frac{P^*}{B_m} \tag{11}$$

From equations (10) and (11), we get

$$\nabla^2 P^* = 0 \tag{12}$$

The following boundary constraints apply to the velocity components.

$$U = 0\ ,\ V = 0,\ W = 0$$

$$\frac{\partial^2 U}{\partial Y^2} = \frac{\partial^2 W}{\partial Y^2} = 0 \text{ at } Y = 0 \tag{13a}$$

$$U = -\rho\frac{\partial U}{\partial Y},\ W = -\sigma\frac{\partial W}{\partial Y},\ \ V = v - V^*$$

$$\frac{\partial^2 U}{\partial Y^2} = \frac{\partial^2 W}{\partial Y^2} = 0 \text{ at } Y = h \tag{13b}$$

Here, ρ represents the slip coefficient at the interface. v refers to the normal approach speed of the surfaces. V^* indicates the normal component of the relative velocity between the fluid and the solid boundary.

The above boundary conditions ensure continuity and compatibility between the fluid and the poroelastic solid at the interface. In particular, the condition accounts for the relative motion between the fluid and the deformable cartilage surface. These boundary conditions are incorporated into the derivation of the modified Reynolds equation (21), thereby preserving the coupled interaction between fluid flow and solid deformation.

Solution of the Problem

The velocity distributions from solving equations (4) and (6), along with the boundary restrictions in (13a) and (13b), are as follows.

$$U = \frac{1}{2\mu_v}\frac{\partial P}{\partial X}\left\{Y\left[(Y-H) - \varsigma H + 2L\varsigma \tanh\left(\frac{H}{2L}\right)\right] + 2L^2\left[1 - \frac{\cosh((2Y-H)/2L^2)}{\cosh(H/2L)}\right]\right\}$$

$$W = \frac{1}{2\mu_v}\frac{\partial P}{\partial Z}\left\{Y\left[(Y-H) - \varsigma H + 2L\varsigma \tanh\left(\frac{H}{2L}\right)\right] + 2L^2\left[1 - \frac{\cosh((2Y-H)/2L^2)}{\cosh(H/2L)}\right]\right\} \tag{14}$$

$$\text{Where, } L = \sqrt{\frac{\eta_c}{\mu_v}}\ ,\ \varsigma = \frac{\rho}{(H+\rho)}\ ,\ \rho = \frac{\beta}{\sqrt{k}}$$

A modified version of the Reynolds equation is created by replacing the velocity expressions in (14) and integrating the continuity relation in (3) across the lubricant film thickness h in the Y -direction.

$$\frac{\partial}{\partial X}\left[F(h,L,\varsigma)\frac{\partial P}{\partial X}\right] + \frac{\partial}{\partial Z}\left[F(h,L,\varsigma)\frac{\partial P}{\partial Z}\right] = 12\mu_v\frac{\partial h}{\partial T} - 12\mu_v (V^*)_{Y=h^*} \tag{15}$$

By integrating equation (12) along the y-direction over the interval $(h, h+h_0)$, we obtain the following expression using the Morgan-Cameron approximation.

$$\left[\frac{\partial P^*}{\partial Y}\right]_{Y=h} = h_0\left[\frac{\partial^2 P^*}{\partial X^2}+\frac{\partial^2 P^*}{\partial Z^2}\right] \tag{16}$$

Equation (7b) can be changed to explain the connection in terms of the relative velocity by leaving out the inertial contributions.

$$\left(\vec{v}^* - \frac{d\vec{W}}{dT}\right) = -K^*\left(\nabla P^* - D\nabla e_{rs}\right) \tag{17}$$

Removing the solid strain, equations (12) and (17) can be combined to create the following expression.

$$\left(\vec{v}^* - \frac{d\vec{W}}{dT}\right) = -K^*\nabla P^*\left(1-\frac{D}{B_m}\right) \tag{18}$$

Equations (12) and (18), along with the constitutive relations in (9), provide a complete set of equations governing the pressure field. P^*, and fluid velocity V^*. Therefore, the system is fully coupled and does not require additional closure relations.

The following is a formula for the fluid velocity that is perpendicular to the cartilage surface.

$$V^* = \left[-K^*\left(1-\frac{D}{B_m}\right)\frac{\partial P^*}{\partial Y}\right]_{V=h} \tag{19}$$

Equations (16) and (19) can be written as

$$V^*\Big|_{Y=h} = -K^*\left(1-\frac{D}{B_m}\right)h_0\left[\frac{\partial^2 P^*}{\partial X^2}+\frac{\partial^2 P^*}{\partial Z^2}\right] \tag{20}$$

The modified Reynolds-type equation can be written in this form by integrating equation (3) over the thickness of the lubricant layer. This involves applying the boundary conditions for V from (13a) and (13b), and replacing the expressions from (14) and (20).

$$\frac{\partial}{\partial X}\left[\left\{F(h,L,\varsigma)-12\mu_v K^* h_0\left(1-\frac{D}{B_m}\right)\right\}\frac{\partial P^*}{\partial X}\right]+\frac{\partial}{\partial Z}\left[\left\{F(h,L,\varsigma)-12\mu_v K^* h_0\left(1-\frac{D}{B_m}\right)\right\}\frac{\partial P^*}{\partial Z}\right]=12\mu_v\frac{\partial h}{\partial T} \tag{21}$$

Where $F(h,L,\varsigma) = h^3(1+3\varsigma) - 6\varsigma L h^2\tanh\left(\frac{h}{2L}\right) - 12L^2 h + 24L^3\tanh\left(\frac{h}{2L}\right)$

$$v = \frac{dh}{dT} = -c\left(\frac{dE}{dT}\right)\cos\theta \tag{22}$$

Let $F(H_s)$ represent the probability density function that describes the random variations of the film thickness H_s. By averaging equation (21) with respect to $F(H_s)$ we obtain the following averaged form.

The random component of the film thickness $H_s(\theta, Z, \varsigma)$, introduced in equation (1), is treated as a stochastic process. After the domain transformation given in (32)–(33), it can be expressed as $h_s(\theta, Z, \varsigma)$ in the transformed coordinates. This stochastic process is defined on a probability space. $(\Omega, \mathcal{F}, \mathbb{P})$, where $\varsigma \in \Omega$, and it is assumed that $h_s \in L^2(\Omega)$, ensuring finite variance and a well-defined expectation.

$$\begin{aligned}&\frac{\partial}{\partial X}\left[\left\{E\left(F(h,L,\varsigma)\right)-12\mu_v K^* h_0\left(1-\frac{D}{B_m}\right)\right\}\frac{\partial E(P^*)}{\partial X}\right]+\\&\frac{\partial}{\partial Z}\left[\left\{E\left(F(h,L,\varsigma)\right)-12\mu_v K^* h_0\left(1-\frac{D}{B_m}\right)\right\}\frac{\partial E(P^*)}{\partial Z}\right]=12\mu_v\frac{\partial h}{\partial T}\end{aligned} \tag{23}$$

The averaging process in equation (23) involves the application of the expectation operator to terms containing spatial derivatives and products of random variables. This requires justification for the interchange of expectation and differentiation. In the present formulation, it is assumed that the random functions involved, such as $h_s(\theta,Z,\varsigma)$ and the pressure field P^*, are sufficiently smooth with respect to the spatial variables and possess finite moments.

Under these assumptions, and since $h_s \in L^2(\Omega)$ Standard results from stochastic analysis ensure that the expectation operator commutes with spatial differentiation. That is,

$$E\left(\frac{\partial P^*}{\partial X}\right)=\frac{\partial}{\partial X}E(P^*),\quad E\left(\frac{\partial P^*}{\partial Z}\right)=\frac{\partial}{\partial Z}E(P^*)$$

This follows from the dominated convergence theorem, provided that the derivatives are bounded in the mean-square sense. Hence, the averaged Reynolds equation (23) is mathematically well-defined.

The expectancy operator is defined as $E(\bullet)$

$$E(\bullet)=\int_{-\infty}^{\infty}(\bullet)F(H_s)dH_s \tag{24}$$

According to Christensen, we take that

$$F(H_s)=\begin{cases}\dfrac{35}{32C^7}\left(C^2-H_s{}^2\right)^3, & -C\le H_s\le C\\ 0, & elsewhere\end{cases} \tag{25}$$

Where $\sigma=C/3$ is the standard deviation.

The probability density function given in equation (25) corresponds to Christensen's stochastic model for surface roughness. This model represents a first-order approximation of the effect of random surface irregularities on the lubricant film thickness.

In this formulation, the roughness function $h_s(\theta,Z,\varsigma)$ is assumed to exhibit small fluctuations about the mean film thickness, and higher-order statistical interactions are neglected. The averaging process is therefore based on the assumption that the roughness amplitude is small compared to the nominal film thickness.

Furthermore, the model assumes that the random roughness is statistically homogeneous and does not introduce long-range correlations in the spatial domain. Under these assumptions, the use of Christensen's distribution provides a tractable and physically reasonable approximation for incorporating surface roughness effects into the Reynolds equation.

The dimensionless quantities are

$$\overline{Z}=\frac{Z}{l}\ ,\ \overline{L}=\frac{L}{c},\ \Psi=\frac{K^{*}h_{0}}{c^{3}},\ \theta=\frac{X}{r}$$

$$\overline{h}=\frac{h}{c}=\overline{H}+\overline{H}_{s}\ ,\ \overline{H}=\frac{H}{c}=1-E\cos\theta\,,\ \overline{H}_{s}=\frac{H_{s}}{c} \tag{26}$$

$$\overline{K}=\frac{K^{*}}{c^{2}},\ \overline{h_{0}}=\frac{h_{0}}{c},\ \overline{P}=\frac{P^{*}c^{2}}{\mu_{v}r^{2}\left(\dfrac{dE}{dT}\right)},\ E=\frac{e_{r}}{c},\ \overline{\rho}=\frac{\rho}{c}$$

$$F(h,L,\varsigma)=c^{3}F(\overline{h},\overline{L},\overline{\varsigma}),\ \lambda=\frac{l}{2r}\ ,\ \overline{c}=\frac{C}{c}$$

The following is the nondimensional version of the modified stochastic Reynolds equation.

$$\frac{\partial}{\partial\theta}\left[\left\{E\left(F(\overline{h},\overline{L},\overline{\varsigma})\right)-12\Psi\left(1-\frac{D}{B_{m}}\right)\right\}\frac{\partial\overline{P}}{\partial\theta}\right]+\frac{1}{4\lambda^{2}}\frac{\partial}{\partial\overline{\overline{Z}}}\left[\left\{E\left(F(\overline{h},\overline{L},\overline{\varsigma})\right)-12\Psi\left(1-\frac{D}{B_{m}}\right)\right\}\frac{\partial\overline{P}}{\partial\overline{\overline{Z}}}\right]=-12\cos\theta \tag{27}$$

Where $F(\overline{h},\overline{L},\overline{\varsigma})=\overline{h}^{3}(1+3\overline{\varsigma})-6\overline{\varsigma}\overline{L}\overline{h}^{2}\tanh\left(\dfrac{\overline{h}}{2\overline{\overline{L}}}\right)-12\overline{L}^{2}\overline{h}+24\overline{L}^{3}\tanh\left(\dfrac{\overline{h}}{2\overline{\overline{L}}}\right)$ (28)

The specific properties of surface roughness affect the terms on the left side of the stochastic Reynolds equation (27). In particular, two types of unidirectional roughness patterns are considered especially significant for theoretical analysis.

The updated Reynolds-type equations for the roughness patterns in the longitudinal and transverse directions can be written as follows after simplification [29]:

$$\frac{\partial}{\partial\theta}\left[\left\{\alpha(\overline{h},\overline{L},\overline{\varsigma})-12\Psi\left(1-\frac{D}{B_{m}}\right)\right\}\frac{\partial\overline{P}}{\partial\theta}\right]+\frac{1}{4\lambda^{2}}\frac{\partial}{\partial\overline{\overline{Z}}}\left[\left\{\beta(\overline{h},\overline{L},\overline{\varsigma})-12\Psi\left(1-\frac{D}{B_{m}}\right)\right\}\frac{\partial\overline{P}}{\partial\overline{\overline{Z}}}\right]=-12\cos\theta \tag{29}$$

Where

$$\alpha(\overline{h},\overline{L},\overline{\varsigma})=\begin{cases}E\left(F(\overline{h},\overline{L},\overline{\varsigma})\right), & longitudinal\\[2mm] \dfrac{1}{E\left(1/F(\overline{h},\overline{L},\overline{\varsigma})\right)}, & Transverse\end{cases}$$

$$\beta(\overline{h},\overline{L},\overline{\varsigma})=\begin{cases}\dfrac{1}{E\left(1/F(\overline{h},\overline{L},\overline{\varsigma})\right)}, & longitudinal\\[2mm] E\left(F(\overline{h},\overline{L},\overline{\varsigma})\right), & Transverse\end{cases}$$

$$\frac{1}{E\left(1/F(\overline{h},\overline{L},\overline{\varsigma})\right)}=\frac{35}{32C^{7}}\int_{-C}^{C}\left(C^{2}-H_{s}^{2}\right)^{3}\times\left(\overline{h}^{3}(1+3\overline{\varsigma})-6\overline{\varsigma}\overline{L}\overline{h}^{2}-12\overline{L}^{2}\overline{h}+24\overline{L}^{3}+\tanh\left(\frac{\overline{h}}{2\overline{\overline{L}}}\right)\right)^{-1}$$

$$E\left(F(\overline{h},\overline{L},\overline{\varsigma})\right)=\overline{h}^{3}(1+3\overline{\varsigma})+\frac{\overline{h}C}{3}-12\overline{L}^{2}\overline{h}+24\overline{L}^{3}-6\overline{\varsigma}\overline{L}\overline{h}^{2}*G$$

$$G=\frac{35}{32C^{7}}\int_{-C}^{C}\left(C^{2}-H_{s}^{2}\right)^{3}\times\tanh\left(\frac{\overline{h}}{2\overline{\overline{L}}}\right)d\overline{H}_{s} \tag{30}$$

Original coordinates are $\overline{P}=0\ at\ \theta=\pm\pi/2$ and $\overline{P}=0\ at\ \overline{Z}=\pm0.5$ (31)

$$\theta \in \left[-\frac{\pi}{2}, \frac{\pi}{2} \right] \text{ and } \overline{Z} \in [-0.5, 0.5]$$

The domain of equation (29) is transformed from its original physical coordinates to a normalised unit square to simplify the numerical solution. Specifically, the variables θ and $\overline{Z}$ are mapped to the interval $[0,1]$. This makes the computational domain dimensionless, which helps in using numerical methods like wavelet-based methods.

$$\overline{S} = \frac{\theta + \pi/2}{\pi} \in [0,1] \text{ and } \bar{t} = \overline{Z} + 1/2 \in [0,1] \tag{32}$$

Transformations are: $\theta = \pi\overline{S} - \frac{\pi}{2}$ and $\overline{Z} = \bar{t} - \frac{1}{2}$ (33)

$$\frac{\partial}{\partial \theta} = \frac{1}{\pi}\frac{\partial}{\partial \overline{S}}, \quad \frac{\partial}{\partial \overline{Z}} = \frac{\partial}{\partial \bar{t}} \text{ and } d\theta d\overline{Z} = \pi\, d\overline{S}\, d\bar{t}$$

$$-12\cos\theta = -12\cos\left(\pi\overline{S} - \frac{\pi}{2}\right) = -12\sin\left(\pi\overline{S}\right)$$

$$H(\theta) = 1 - E\cos\theta$$

$$H(\overline{S}) = 1 - E\cos\left(\pi\overline{S} - \frac{\pi}{2}\right) = 1 - \varepsilon\sin\left(\pi\overline{S}\right) \tag{34}$$

After the domain transformation for equation (28) is given by

$$\frac{1}{\pi^2}\frac{\partial}{\partial \overline{S}}\left[\left\{\alpha(\bar{h}, \overline{L}, \bar{\varsigma}) - 12\Psi\left(1 - \frac{D}{B_m}\right)\right\}\frac{\partial \overline{P}}{\partial \overline{S}}\right] + \frac{1}{4\lambda^2}\frac{\partial}{\partial \bar{t}}\left[\left\{\beta(\bar{h}, \overline{L}, \bar{\varsigma}) - 12\Psi\left(1 - \frac{D}{B_m}\right)\right\}\frac{\partial \overline{P}}{\partial \bar{t}}\right] = -12\cos(\pi\overline{S}) \tag{35}$$

Where, $\overline{S}, \bar{t} \in [0,1]$

The Reynolds boundary conditions are used to calculate the film pressure distribution from the stochastic generalised Reynolds equation (35).

$$\overline{P}(0,\bar{t}) = 0,\ \overline{P}(1,\bar{t}) = 0 \text{ and } \overline{P}(\overline{S},0) = 0,\ \overline{P}(\overline{S},1) = 0 \tag{36}$$

Load carrying capacity

After applying the domain transformation, the bearing's load-carrying capacity W, which comes from the pressure inside the lubricant film, is calculated as follows.

$$W = -\pi l r \int_0^1\int_0^1 E\left(P^*\right)\sin\left(\pi S\right) dS\, dt \tag{37}$$

The dimensionless load-carrying capacity of a poroelastic partial journal bearing can be expressed over the normalised unit-square domain after applying the domain transformation.

$$\overline{W} = \pi\sum_{i=0}^{I}\sum_{j=0}^{I}\overline{P}_{i,j}\sin(\pi\overline{S})\, d\overline{S}\, d\bar{t} \tag{38}$$

Time height

Non-dimensional response time is given by $\tau = \left(\dfrac{Wc^2}{\eta l r^3}\right)$ (39)

The time required for the journal to change from $E = 0$ to $E = 1$ is used to calculate the time-height relationship, according to equation (40).

$$\frac{dE}{d\tau} = \frac{1}{f(E,L,\Psi)}$$

$$f(E,L,\Psi) = \pi\sum_{i,j}\overline{P}_{i,j}\sin(\pi\overline{S})d\overline{S}\,d\overline{t} \tag{40}$$

III. Basic Properties of Sine Cosine Wavelet

Definition of wavelet and Sine and cosine wavelets

$\psi_{s,t}(r) = \psi(s,b,t,r)$ be the sine cosine wavelet, which has four arguments $s = 0,1,2,...,2^b - 1$, $b = 0,1,2,...$, where t is given in equation (42), and r is normalised time. Which is defined in the interval $[0,1)$ as [XXV]:

$$\psi_{s,t}(r) = \begin{cases} 2^{b+1/2} g_t(2^b r - s) \ for \ \dfrac{s}{2^b} \le r \le \dfrac{s+1}{2^b} \\ 0 \qquad\qquad otherwise \end{cases} \tag{41}$$

with

$$g_t(r) = \begin{cases} 1/\sqrt{2} & t = 0 \\ \cos(2t\pi r) & t = 1,2,...,l \\ \sin(2(t-l)\pi r & t = l+1, l+2,...,2l \end{cases} \tag{42}$$

Where l is a positive integer. This set of wavelets is an orthonormal set.

Function approximation

Let $g(r)$ be any function defined over the interval of $[0,1)$ that is expressed as

$$g(r) = \sum_{t=0}^{\infty}\sum_{s=0}^{2^b-1} k_{s,t}\psi_{s,t}(r) \tag{43}$$

$$\text{Where } K = \langle g(r), \psi_{s,t}(r)\rangle \tag{44}$$

By eliminating the infinite series equation (43) at the level $t = 2l$ and $s = 2^b - 1$.
Now, an approximate representation for $g(r)$ as

$$g(r) = \sum_{t=0}^{2l}\sum_{s=0}^{2^b-1} k_{s,t}\psi_{s,t}(r) = K^T\psi(r) \tag{45}$$

where the matrices K and $\psi(r)$ are $2^b(2l+1)\times 1$ matrices given by

$$K = \left[k_{0,0}, k_{0,1},...,k_{0,2l}, k_{1,0}, k_{1,2l},...,k_{2^b-1,0},...,k_{2^b-1,2l}\right]^T \tag{46}$$

$$\psi(r) = \left[\psi_{0,0}, \psi_{0,1},...,\psi_{0,2l}, \psi_{1,0}, \psi_{1,2l},...,\psi_{2^b-1,0},...,\psi_{2^b-1,2l}\right]^T \tag{47}$$

Sine- cosine wavelet operational matrix of integration method

Let us derive the operational matrix of integration first matrix p with $l = 2$ and $b = 1$. We obtained 10 basis function are: [XI]:

$$\left.\begin{aligned} \psi_{0,0}(r) &= \sqrt{2} \\ \psi_{0,1}(r) &= 2\cos(4\pi r) \\ \psi_{0,2}(r) &= 2\cos(8\pi r) \\ \psi_{0,3}(r) &= 2\sin(4\pi r) \\ \psi_{0,4}(r) &= 2\sin(8\pi r) \end{aligned}\right\} \; 0 \le r \le 0.5 \tag{48}$$

and

$$\left.\begin{aligned} \psi_{1,0}(r) &= \sqrt{2} \\ \psi_{1,1}(r) &= 2\cos(2\pi(2r-1)) \\ \psi_{1,2}(r) &= 2\cos(4\pi(2r-1)) \\ \psi_{1,3}(r) &= 2\sin(2\pi(2r-1)) \\ \psi_{1,4}(r) &= 2\sin(4\pi(2r-1)) \end{aligned}\right\} \; 0.5 \le r \le 1 \tag{49}$$

By integrating equation (48) from 0 to r and using equation (44)

$$\int_0^r \psi_{10}(r)dr = p_{10}\psi_{10}(r) \tag{50}$$

$$p_{10\times10} = \begin{bmatrix} 0.25 & 0 & 0 & -0.15923 & -0.0796 & 0.5 & 0 & 0 & 0 & 0 \\ 0 & 0 & 0 & -0.0796 & 0 & 0 & 0 & 0 & 0 & 0 \\ 0 & 0 & 0 & 0 & 0.039808 & 0 & 0 & 0 & 0 & 0 \\ 0.0796 & -0.0796 & 0 & 0 & 0 & 0 & 0 & 0 & 0 & 0 \\ 0.039808 & 0 & -0.039808 & 0 & 0 & 0 & 0 & 0 & 0 & 0 \\ 0 & 0 & 0 & 0 & 0 & 0.25 & 0 & 0 & -0.15923 & -0.0796 \\ 0 & 0 & 0 & 0 & 0 & 0 & 0 & 0 & -0.0796 & 0 \\ 0 & 0 & 0 & 0 & 0 & 0 & 0 & 0 & 0 & 0.39808 \\ 0 & 0 & 0 & 0 & 0 & 0.0796 & -0.0796 & 0 & 0 & 0 \\ 0 & 0 & 0 & 0 & 0 & 0.039808 & 0 & -0.039808 & 0 & 0 \end{bmatrix}$$

We obtained $\psi_{10}(r) = \left[\psi_{0,0}, \psi_{0,1}, \psi_{0,2}, \psi_{0,3}, \psi_{0,4}, \psi_{1,0}, \psi_{1,1}, \psi_{1,2}, \psi_{1,3}, \psi_{1,4}\right]^T$ (51)

Similarly, integrating the equation again and again, we can get p^2 and p^3

$$\int_0^r\int_0^r \psi_{10}(r)dr = p_{10}^2\psi_{10}(r) \tag{52}$$

$$\int_0^r\int_0^r\int_0^r \psi_{10}(r)dr = p_{10}^3\psi_{10}(r) \tag{53}$$

A Stability and Convergence Analysis of the Proposed Method

In this section, the convergence and stability of the sine–cosine wavelet operational matrix method applied to equation (35) are discussed.

Error Estimate

Let $\overline{P}(\overline{S},\overline{t})$ denote the exact solution of the transformed Reynolds equation (35), and let $\overline{P_N}(\overline{S},\overline{t})$ be its wavelet approximation obtained using a finite number of sine - cosine wavelets as defined in (45). Then, for sufficiently smooth $\overline{P}(\overline{S},\overline{t})$, the approximation satisfies:

$$\left\|\overline{P}(\overline{S},\overline{t})-\overline{P_N}(\overline{S},\overline{t})\right\|_2 \le C(2^b)^{-k}$$

where C is a constant independent of b and k depends on the smoothness of $\overline{P}(\overline{S},\overline{t})$. Thus, the approximation error decreases as the level of resolution increases. b increases.

Convergence

Since the sine–cosine wavelets $\psi_{s,t}$ form an orthonormal basis on $[0,1)$, the expansion given in (43) converges to $g(r)$ in the L^2-sense. Extending this result to two dimensions, the approximate pressure converges to the exact solution $\overline{P}(\overline{S},\overline{t})$ of equations (35) as $b \to \infty$, i.e., $\lim_{b\to\infty}\overline{P_N}(\overline{S},\overline{t})=\overline{P}(\overline{S},\overline{t})$.

Stability of the Collocation Scheme

By substituting the wavelet expansion into equation (35) and applying the operational matrix of integration, the governing equation is reduced to a system of linear algebraic equations of the form $AX = B$.

where A is the coefficient matrix depending on $F(\overline{h},\overline{L},\overline{\varsigma})$, K, and wavelet basis functions, and X is the vector of unknown coefficients.

Due to the orthogonality and boundedness of the sine - cosine wavelet basis, the matrix A remains well-conditioned for moderate values of b. Hence, the numerical scheme is stable, and small perturbations in input or truncation errors do not lead to significant deviations in the computed solution.

Theorems and Lemmas

Lemma 1: If the two-dimensional sine cosine wavelet expansion of a continuous function $g(r)$ converges uniformly on $[0,1]\times[0,1]$ Then the sine-cosine wavelet expansion converges to the function. $g(r)$ i.e., $g(x,y)=g(r)$ [XXXI].

Proof: Let $$f(r)=\sum_{s_1=0}^{\infty}\sum_{t_1=0}^{\infty}\sum_{s_2=0}^{\infty}\sum_{t_2=0}^{\infty}k_{s_1,t_1,s_2,t_2}\psi_{s_1,t_1}(x)\psi_{s_2,t_2}(y) \tag{54}$$

Where $$k_{s_1,t_1,s_2,t_2}=\int_0^1\int_0^1\psi_{c,d}(x)\psi_{u,v}(y)g(x,y)\,dx\,dy \text{ and } g(x,y)=g(r) \tag{55}$$

Multiply both sides of equation (54) by $\psi_{c,d}(x)\psi_{u,v}(y)$, where c,d,u,v are fixed, integrating term-wise $[0,1]\times[0,1]$.

We obtain

$$\int_0^1\int_0^1 \psi_{c,d}(x)\psi_{u,v}(y)f(r)dx\,dy = \int_0^1\int_0^1 \sum_{s_1,t_1,s_2,t_2} k_{s_1,t_1,s_2,t_2}\psi_{s_1,t_1}(x)\psi_{s_2,t_2}(y)\psi_{c,d}(x)\psi_{u,v}(y)\,dx\,dy \tag{56}$$

Interchanging summation and integration yields

$$= \sum_{s_1,t_1,s_2,t_2} k_{s_1,t_1,s_2,t_2}\left(\int_0^1\left(\psi_{s_1,t_1}(x)\psi_{c,d}(x)\right)dx\right)\left(\int_0^1\left(\psi_{s_2,t_2}(y)\psi_{u,v}(y)\right)dy\right) \tag{57}$$

Using the orthonormality of the sine-cosine wavelet basis

$$\int_0^1\left(\psi_{s_1,t_1}(x)\psi_{c,d}(x)\right)dx = \delta_{s_1,c}\delta_{t_1,d} \quad \text{and} \quad \int_0^1\left(\psi_{s_2,t_2}(y)\psi_{u,v}(y)\right)dy = \delta_{s_2,u}\delta_{t_2,v}$$

Equation (57) reduces to $\int_0^1\int_0^1 \psi_{c,d}(x)\psi_{u,v}(y)f(x,y)dx\,dy = k_{c,d,u,v}$ (58)

Here, $k_{s_1,t_1,s_2,t_2} = (g(x,y)\psi_{s_1,t_1}(x)\psi_{s_2,t_2}(y))$, $s_1,t_1,s_2,t_2 \in \square$

The function $g(x,y)$ and $f(x,y)$ have the same Fourier expansions with respect to the two-dimensional sine - cosine wavelet basis, and consequently $g(x,y)=f(x,y)$.

Theorem 1. Let $g(x,y)=\square^2\left[[0,1]\times[0,1]\right]$ satisfy Lemma 1.

Let $\hat{g}_{\square}(x,y)=\sum_{s_1,t_1,s_2,t_2} k_{s_1,t_1,s_2,t_2}\psi_{s_1,t_1}(x)\psi_{s_2,t_2}(y)$ denote the N-Partial sum of the two dimensional sine cosine wavelet expansion, then the sequence $\{\hat{g}_{\square}\}$ in uniformly Cauchy on $[0,1]\times[0,1]$.

Proof: From Lemma 1, the two-dimensional sine cosine wavelet expansion of $g(x,y)$ converges uniformly on $[0,1]\times[0,1]$ uniform converges implies that the sequence of partial sums is a uniform Cauchy hence for every $\varepsilon>0$ there exists N_0 such that for all $F,G\geq N_0$, then $\left\|\hat{g}_F-\hat{g}_G\right\|_{L^\infty}<\infty$ (59)

Hence the proof.

Theorem 2. Let $g(x,y)=\square^2\left[[0,1]\times[0,1]\right]$ satisfy Lemma 1.

Let $\hat{g}(x,y)=\sum_{s_1,t_1,s_2,t_2} k_{s_1,t_1,s_2,t_2}\psi_{s_1,t_1}(x)\psi_{s_2,t_2}(y)$ be the N-th partial sum of its two-dimensional sine -cosine wavelet expansion, the

$$\lim_{N\to\infty}\int_0^1\int_0^1 \hat{g}_{\square}(x,y)\,dx\,dy = \int_0^1\int_0^1 \hat{g}_{\square}(x,y)\,dx\,dy \tag{60}$$

Proof: By Lemma 1, the sequence $\{\hat{g}_{\square}\}$ uniformly converges to $g(x,y)$ on $[0,1]\times[0,1]$ uniformly implies convergence in $L^1\left([0,1]^2\right)$.

$$\lim_{N\to\infty}\int_0^1\int_0^1 \hat{g}_{\square}(x,y)\,dx\,dy = \int_0^1\int_0^1 \lim_{N\to\infty}\hat{g}_{\square}(x,y)\,dx\,dy \tag{61}$$

$$=\int_0^1\int_0^1 g(x,y)\,dx\,dy$$

Method of Implementation

The general elliptical partial differential equation of the form

$$o_1(x,y)\frac{\partial^2 P}{\partial x^2}+o_2(x,y)\frac{\partial^2 P}{\partial y^2}+o_3(x,y)\frac{\partial P}{\partial x}+o_4(x,y)\frac{\partial P}{\partial y}+o_5(x,y)P=q(x,y) \quad (62)$$

Where $o_1,o_2,o_3,...,o_5$ and q be any functions of x and y or constants. The computational domain of equation (62) is $[0,1]\times[0,1]$.

We considered that the second-order partial derivative can be expressed by a sine-cosine wavelet series given by [II].

$$\frac{\partial^2 P}{\partial x^2}=\sum_{t=1}^{2I}\sum_{s=1}^{2I}\alpha_{s,t}sc_s(x)sc_t(y) \quad (63)$$

$$\frac{\partial^2 P}{\partial y^2}=\sum_{t=1}^{2I}\sum_{s=1}^{2I}\beta_{s,t}sc_s(x)sc_t(y) \quad (64)$$

The definition of collocation points is

$$x_{cp}=\frac{cp-0.5}{2I},\ cp=1,2,....,2I \text{ and } y_{cp}=\frac{cp-0.5}{2I},\ cp=1,2,....,2I$$

Let us consider the Dirichlet boundary conditions.

$$P(0,y)=0=g(0,y),\ P(1,y)=0=g(1,y),$$
$$P(x,0)=0=g(x,0) \text{ and } P(x,1)=0=g(x,1) \quad (65)$$

From equations (63) and (64), we get the expression:

$$\frac{\partial P}{\partial x}=g(1,y)-g(0,y)+\sum_{t=1}^{2I}\sum_{s=1}^{2I}\alpha_{s,t}\left(p_{s,1}(x)-k_{s,1}\right)sc_t(y) \quad (66)$$

$$P(x,y)=g(0,y)+x(g(1,y)-g(0,y))+\sum_{t=1}^{2I}\sum_{s=1}^{2I}\alpha_{s,t}\left(p_{s,2}(x)-xk_{s,1}\right)sc_t(y) \quad (67)$$

$$\frac{\partial P}{\partial y}=g(x,1)-g(x,0)+\sum_{t=1}^{2I}\sum_{s=1}^{2I}\beta_{s,t}\left(p_{t,1}(y)-k_{t,1}\right)sc_s(x) \quad (68)$$

$$P(x,y)=g(x,0)+y(g(x,1)-g(x,0))+\sum_{t=1}^{2I}\sum_{s=1}^{2I}\beta_{s,t}\left(p_{t,2}(y)-yk_{t,1}\right)sc_s(x) \quad (69)$$

A system of $4I^2$ equations is created by setting Eqs. (67) and (69) are equal, and using the collocation points. Substituting the formulas for $P(x,y)$ and its partial derivatives into the main differential equation (62) gives us an additional set of $4I^2$ equations. To find the unknown Haar coefficients $\alpha_{s,t}$ and $\beta_{s,t}$ these two systems are solved together. Once we know the coefficients, we can easily put them into either Eq. (67) or Eq. (69) to get the approximate solution.

Test Problem

Consider a linear Boundary value problem. $-y'' = (2-4x^2)y$ with Neumann boundary conditions $y'(0)=0$ and $y'(1)=-1/4$ with an exact solution $y(x)=e^{-x^2}$.

Solution:

Table 1: Solution of FDM versus SCWOMM

Sl. No.	x	Exact Solution	FDM Solution	SCWOMM Solution	FDM Error	SCWOMM Error
1	0.0000	1.000000	0.997029	1.000000	2.971021e-03	00000000
2	0.0625	0.996101	0.993180	0.996101	2.921690e-03	00000000
3	0.1250	0.984496	0.981632	0.984496	2.864653e-03	00000000
4	0.1875	0.965455	0.962655	0.965455	2.800006e-03	00000000
5	0.2500	0.939413	0.936685	0.939413	2.727692e-03	00000000
6	0.3125	0.906961	0.904313	0.906961	2.647545e-03	00000000
7	0.3750	0.868815	0.866256	0.868815	2.559354e-03	00000000
8	0.4375	0.825797	0.823334	0.825797	2.462938e-03	00000000
9	0.5000	0.778801	0.776443	0.778801	2.358215e-03	00000000
10	0.5625	0.728763	0.726518	0.728763	2.245274e-03	00000000
11	0.6250	0.676634	0.674509	0.676634	2.124430e-03	00000000
12	0.6875	0.623344	0.621348	0.623344	1.996259e-03	00000000
13	0.7500	0.569783	0.567921	0.569783	1.861610e-03	00000000
14	0.8125	0.516771	0.515049	0.516771	1.721592e-03	00000000
15	0.8750	0.465043	0.463466	0.465043	1.577542e-03	00000000
16	0.9375	0.415237	0.413806	0.415237	1.430963e-03	00000000
17	1.0000	0.367879	0.366596	0.367879	1.283456e-03	00000000

It serves to emphasise the effectiveness and correctness of the methods employed. The solution given by FDM is close to that of the exact solution, within a maximum permissible error of 2.97×10^{-3}, in comparison, yields machine precision accuracy for the SCWOMM approach. Thus, it has been shown that wavelet-based operational matrices provide an exact, accurate, efficient, and reliable alternative approach for solving nonlinear BVP problems, even using collocation points.

IV. Results and Discussion

Pressure

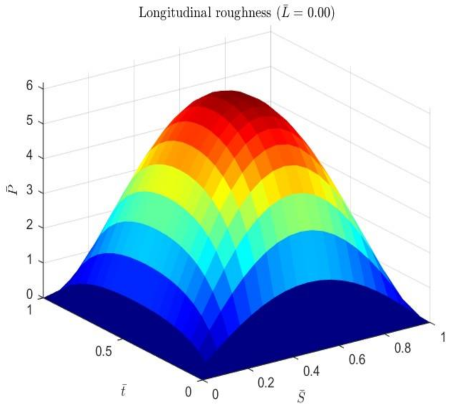

Fig.3.

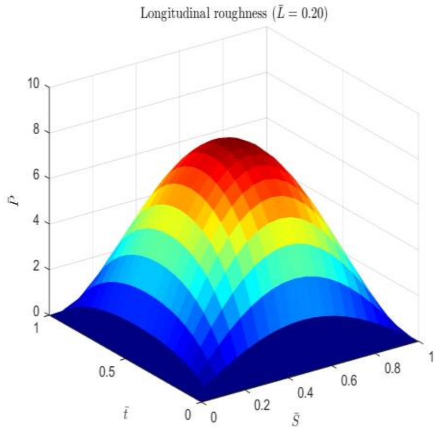

Fig.4.

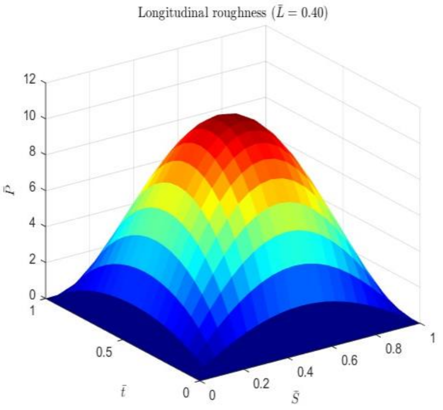

Fig.5.

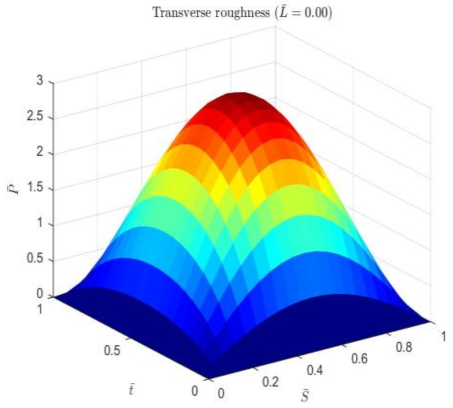

Fig.6.

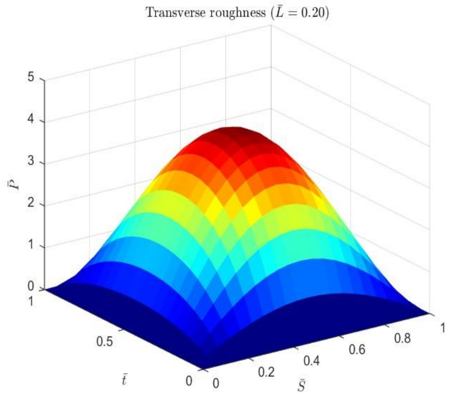

Fig. 7.

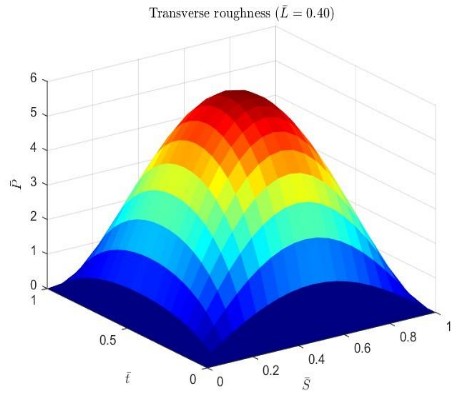

Fig. 8.

Fig. 3 to 8 shows how nondimensional pressure changes along the circumferential coordinate for different values of the Couple stress parameter. $\bar{L}$, with $E = 0.3$, $\bar{\rho} = 0.3$, $\lambda = 1.5$, $\bar{C} = 0.2$, and $\frac{D}{B_m} = 0.3$ for both longitudinal and transverse roughness patterns $\bar{K} = 7.65 \times 10^{-5}$.

Compared to the Newtonian limit ($\bar{L} \to 0$), increasing the Couple stress parameter leads to a significant rise in pressure for both roughness types. The increase in pressure for the longitudinal roughness pattern is more pronounced than for the transverse pattern. This pattern indicates that the joint's ability to carry load increases due to the microstructural effects of the synovial fluid, represented by Couple stresses. The physical resistance of long-chain hyaluronic acid molecules to deformation causes the lubricating film's pressure to rise during the squeezing motion.

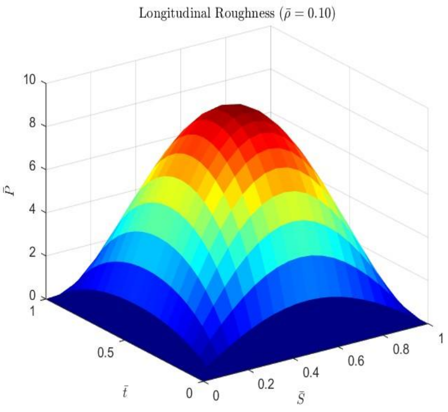

Fig. 9.

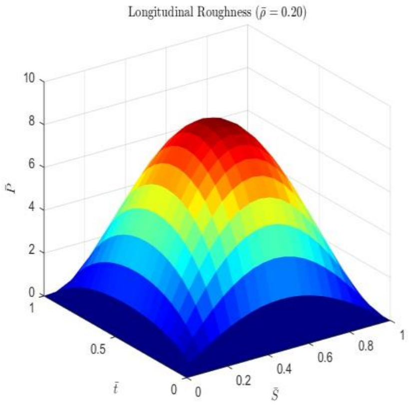

Fig. 10.

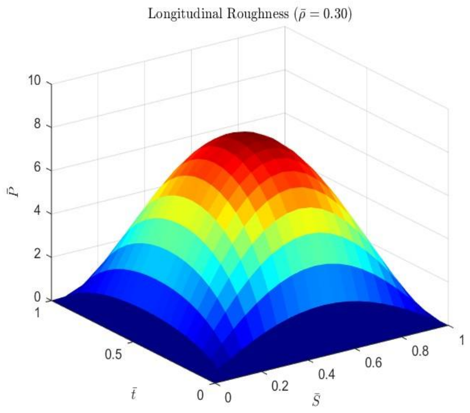

Fig. 11.

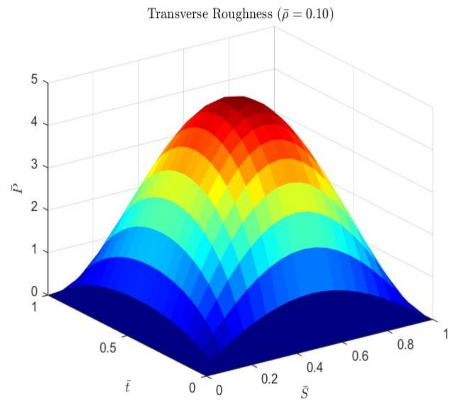

Fig. 12.

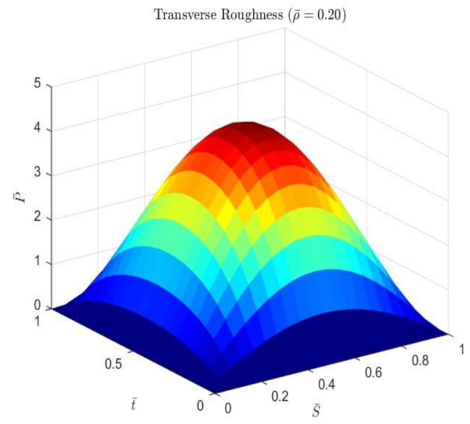

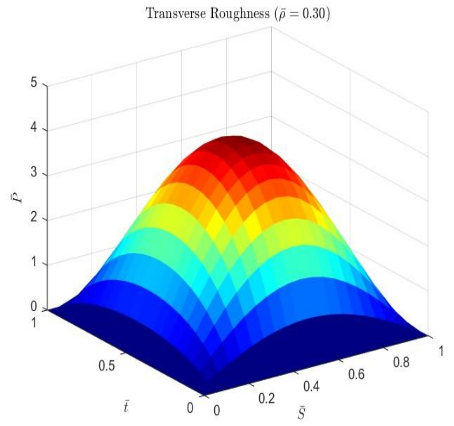

sss

Fig. 13.

Fig. 14.

Fig. 9 to 14. The pressure distribution along $\overline{S}$ with the variable slip parameter $\overline{\rho}$ is shown here, $E = 0.3$, $\overline{C} = 0.2$, $\lambda = 1.5$, $\overline{L} = 0.4$, $\frac{D}{B_m} = 0.3$, and $\overline{K} = 7.65 \times 10^{-5}$.

For both longitudinal and transverse roughness patterns, the nondimensional pressure $\overline{P}$ decreases as $\overline{\rho}$ increases. This means that smoother movement between the cartilage surfaces is possible due to higher slip velocity and porous boundary conditions, which reduce resistance in the fluid layer. This behaviour matches physiological findings that slipping at the cartilage fluid interface helps hip joints work effectively, especially under high load conditions.

Load Carrying Capacity

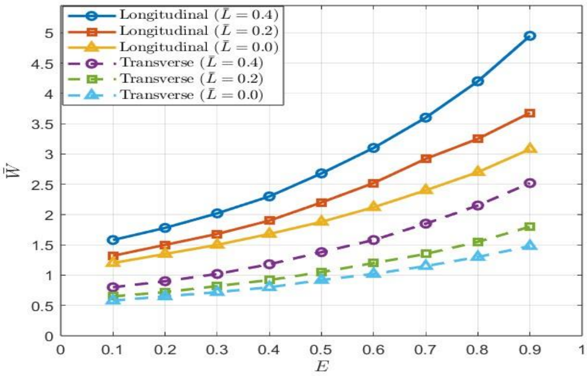

Fig. 15: **N**ondimensional load-carrying capacity $\overline{W}$ in relation to the eccentricity ratio E.

For both longitudinal and transverse roughness patterns, Fig. 15 shows that. $\overline{W}$ increases as $\overline{L}$ increases. Unlike the Newtonian case $\overline{L} = 0$, the presence of Couple stresses counters the squeezing action. This raises film pressure and, therefore, the load-carrying capacity.

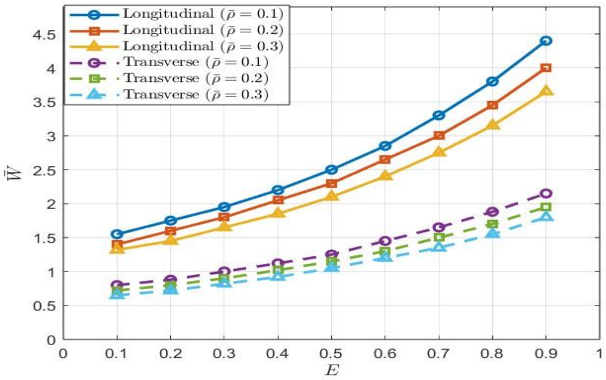

Fig. 16: Nondimensional load-carrying capacity $\overline{W}$ in relation to the eccentricity ratio E.

Fig. 16 shows that when $\bar{\rho}$ increases, $\bar{W}$ drops. Longitudinal roughness can support a larger load, but the decrease is more noticeable with transverse roughness. This trend indicates that higher slip encourages relative surface motion, which reduces fluid film pressure buildup.

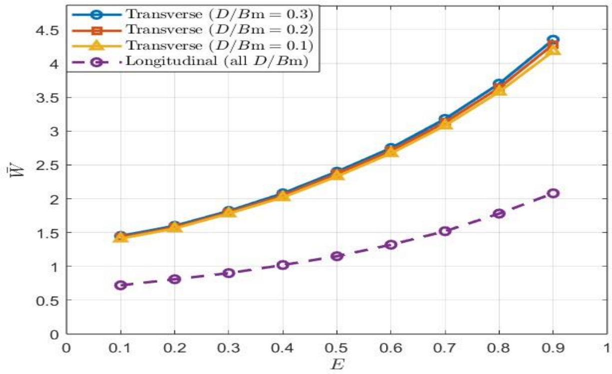

Fig. 17: **N**ondimensional load-carrying capacity $\bar{W}$ in relation to the eccentricity ratio E.

Both roughness patterns illustrate that. $\bar{W}$ increases with ε but decreases as $\frac{D}{B_m}$ rises.

The load-carrying ability of longitudinal roughness is always greater than that of transverse roughness. Greater compliance lowers film pressure by decreasing resistance to squeezing.

Time height relation

A key factor in designing bearings and lubricating joints is the response time. τ of the squeezing film.

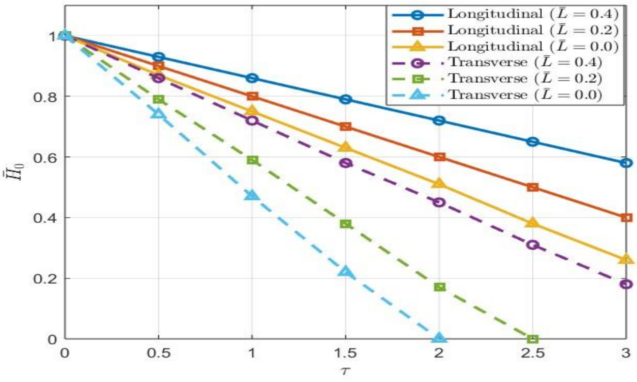

Fig. 18: Non-dimensional time height for different values of $\bar{L}$

For both longitudinal and transverse roughness patterns, Fig. 18 shows that. τ increases as $\bar{L}$ rises. The effects of the Couple stress fluid at the microstructural level play a role here. Higher concentrations of hyaluronic acid molecules resist film compression and lead to slower film draining compared to the Newtonian situation $\bar{L} = 0$. This change is what improves response time.

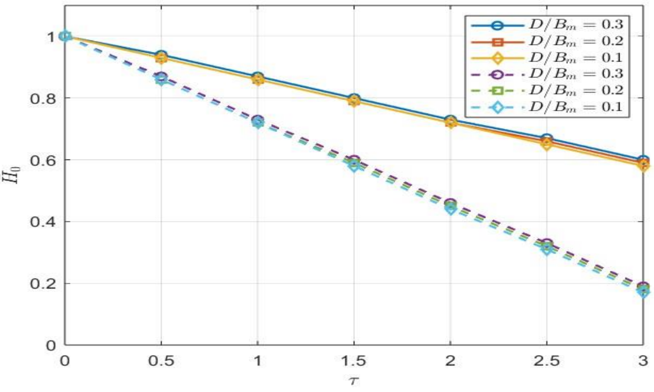

Fig. 19: Non-dimensional time height for different values $\frac{D}{B_m}$.

Fig. 19 shows that for both roughness patterns, τ decreases as increases. This suggests that stiffer cartilage shortens the film's thinning time. Significantly longer response times occur with lower values of $\frac{D}{B_m}$, which indicates worse cartilage. Additionally, higher permeability $\bar{K}$ increases fluid exudation through the porous cartilage matrix, which speeds up film drainage.

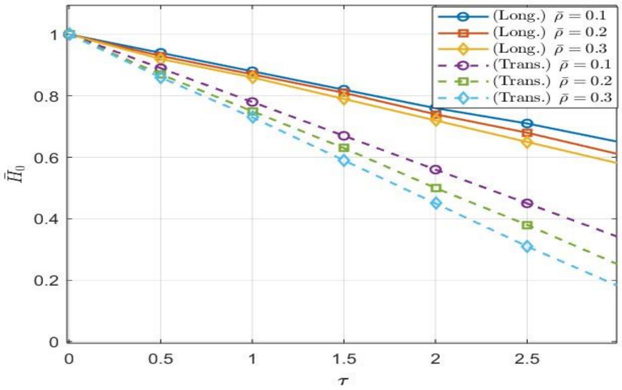

Fig. 20: Non-dimensional time height for different $\bar{\rho}$

For both longitudinal and transverse roughness, Fig. 20 shows that. τ decreases as $\bar{\rho}$ increases. The physiological findings of effective joint lubrication under sliding conditions match with higher slip at the porous boundary. This promotes fluid motion and shortens the time for the film to reach its minimum height.

A couple of stresses greatly improve film support. Longitudinal roughness provides a better load-carrying capability. Higher cartilage compliance and slip reduce $\bar{W}$. This highlights the importance of boundary conditions and material properties. The wavelet-based operational matrix approach captures these patterns well and effectively captures the dynamic changes in film thickness. The Couple stress parameter and cartilage characteristics have the biggest impact on response time. It provides precise and reliable solutions for difficult two-dimensional lubrication problems in hip joint biomechanics in both pathological and dynamic loading situations.

V. Conclusions

By focusing on hip joint lubrication, this paper looks at the squeeze film behaviour of finite rough poroelastic partial journal bearings that are lubricated by couple stress fluids. The governing equations are solved effectively using a sine-cosine wavelet operational matrix of integration approach, along with domain transformation. These equations consider cartilage poroelasticity, random surface roughness, and the effects of couple stress fluids.

A summary of the key findings: Couple Stress Effects: Compared to the Newtonian case, couple stress fluids increase the squeeze film response time and improve the load-carrying capacity. This is because fluid microstructures, such as molecules of hyaluronic acid, resist film compression.

Surface Roughness Influence: Compared to the smooth surface case, longitudinal roughness improves load-carrying capacity and response time. In contrast, transverse roughness slightly reduces these qualities. The results show how crucial surface topography is in managing joint lubrication.

Numerical Methodology: The wavelet-based operational matrix technique effectively captures both dynamic and steady state behaviour using fewer basis functions. This method provides precise, reliable, and cost-effective solutions for two-dimensional lubrication problems.

Biomechanical Implications: The proposed model accurately predicts key lubrication properties. This allows for selecting the best design parameters for prosthetic joints and offers insights into the function of natural hip joints under various surface and fluid conditions.

This work is different from earlier research because it combines sine-cosine wavelet operational matrices with domain transformation. It also includes strong theoretical guarantees, such as uniqueness, uniform convergence, and the validity of term-wise integration. This approach provides a trustworthy and effective framework for studying how surface roughness, Couple stress fluids, and poroelasticity influence synovial joint lubrication.

Conflict of Interest

There was no relevant conflict of interest regarding this paper.

References

I. Ateshian, G. A., and C. T. Hung. "The Natural Synovial Joint: Properties of Cartilage." Proceedings of the Institution of Mechanical Engineers, Part J: Journal of Engineering Tribology, vol. 220, no. 8, 2006, pp. 657–670. 10.1243/13506501JET86

II. Aziz, I., Siraj-ul-Islam, and B. Šarler. "Wavelets Collocation Methods for the Numerical Solution of Elliptic Boundary Value Problems." Computer Methods in Applied Mechanics and Engineering, vol. 197, no. 3-4, 2008, pp. 346–358. 10.1016/j.apm.2012.02.046

III. Bujurke, N. M., S. G. Bhavi, and N. B. Naduvinamani. “The Effect of Couple Stresses in Squeeze Film Poro-Elastic Bearings with Special Reference to Synovial Joints.” IMA Journal of Mathematics Applied in Medicine and Biology, vol. 7, no. 4, 1990, pp. 231–243. 10.1093/imammb/7.4.231

III. Bujurke, N. M., and R. B. Kudenatti. “An Analysis of Rough Poroelastic Bearings with Reference to Lubrication Mechanism of Synovial Joints.” Applied Mathematics and Computation, vol. 178, no. 2, 2006, pp. 309–320. 10.1016/j.amc.2005.11.048

IV. Bujurke, N. M., R. B. Kudenatti, and V. B. Awati. “Effect of Surface Roughness on Squeeze Film Poroelastic Bearings with Special Reference to Synovial Joints.” Mathematical Biosciences, vol. 209, no. 1, 2007, pp. 76–89. 10.1016/j.mbs.2007.01.002

V. Christensen, H. “Stochastic Models of Hydrodynamic Lubrication of Rough Surfaces.” Proceedings of the Institution of Mechanical Engineers, vol. 184, no. 55, 1970, pp. 1013–1026. 10.1243/PIME_PROC_1969_184_074_02

VI. Higginson, G. R., and R. Norman. “The Lubrication of Porous Elastic Solids with Reference to the Functioning of Human Joints.” Journal of Mechanical Engineering Science, vol. 16, no. 4, 1974, pp. 250–257. 10.1243/JMES_JOUR_1974_016_045_02

VII. Hlaváček, M. “Lubrication of the Human Ankle Joint in Walking with the Synovial Fluid Filtrated by the Cartilage with the Surface Zone Worn Out.” Journal of Biomechanics, vol. 32, no. 10, 1999, pp. 1059–1069. 10.1016/S0021-9290(99)00095-0

VIII. Hlaváček, M. “The Influence of the Acetabular Labrum Seal, Intact Articular Superficial Zone and Synovial Fluid Thixotropy on Squeeze-Film Lubrication of a Spherical Synovial Joint.” Journal of Biomechanics, vol. 35, no. 10, 2002, pp. 1325–1335. 10.1016/S0021-9290(02)00172-0

IX. Hori, R. Y., and L. F. Mockros. “Indentation Tests of Human Articular Cartilage.” Journal of Biomechanics, vol. 9, no. 4, 1976, pp. 259–268. 10.1016/0021-9290(76)90012-9

X. Irfan, N., and S. Kapoor. “Quick Glance on Different Wavelets and Their Operational Matrix Properties.” Alexandria Engineering Journal, vol. 57, no. 4, 2018, pp. 3519–3533. 10.1016/j.aej.2017.12.006

XI. Jin, Z. M., D. Dowson, and J. Fisher. “Effect of Porosity of Articular Cartilage on the Lubrication of a Normal Human Hip Joint.” Proceedings of the Institution of Mechanical Engineers, Part H: Journal of Engineering in Medicine, vol. 206, no. 3, 1992, pp. 117–124. 10.1243/PIME_PROC_1992_206_279_02

XII. Lin, J.-R., W.-H. Liao, and C.-R. Hung. “The Effects of Couple Stresses in the Squeeze Film Characteristics between a Cylinder and a Plane Surface.” Journal of Marine Science and Technology, vol. 12, no. 2, 2004, pp. 119–123. https://jmstt.ntou.edu.tw/journal/vol12/iss2/7

XIII. Mow, V. C., and H. Rik. Basic Orthopaedic Biomechanics and Mechano-Biology. 3rd ed., Lippincott Williams & Wilkins, 2005.

XIV. Mow, V. C., and W. M. Lai. “Recent Development in Synovial Joint Biomechanics.” SIAM Review, vol. 22, no. 3, 1980, pp. 275–317. 10.1137/1022056

XV. Nabhani, M., M. El Khilfi, and B. Bou-Said. “Non-Newtonian Couple Stresses Poroelastic Squeeze Film.” Tribology International, vol. 64, 2013, pp. 116–127. 10.1016/j.triboint.2013.03.006

XVI. Naduvinamani, N. B., and S. Santosh. “Micropolar Fluid Squeeze Film Lubrication of Finite Porous Journal Bearing.” Proceedings of the 13th Asian Congress of Fluid Mechanics, Dhaka, Bangladesh, 2010, pp. 970–973. 10.1016/j.triboint.2010.11.019

XVII. Naduvinamani, N. B., and G. K. Savitramma. “Micropolar Fluid Squeeze Film Lubrication between Rough Anisotropic Poroelastic Rectangular Plates.” Tribology, Materials, Surfaces & Interfaces, vol. 6, no. 4, 2012, pp. 174–181. 10.1179/1751584X12Y.0000000021

XVIII. Naduvinamani, N. B., and G. K. Savitramma. “Effect of Surface Roughness on the Squeeze Film Lubrication of Finite Poroelastic Partial Journal Bearings with Couple Stress Fluids.” Tribology International, vol. 43, no. 11, 2010, pp. 2083–2094. 10.1155/2014/690147

XIX. Nordin, M., and V. Frankel. Basic Biomechanics of the Musculoskeletal System. 3rd ed., Lippincott Williams & Wilkins, 2001.

XX. Prakash, J., and K. Tiwari. “Effect of Surface Roughness on the Squeeze Film between Rotating Porous Annular Discs with Arbitrary Porous Wall Thickness.” International Journal of Mechanical Sciences, vol. 27, no. 3, 1985, pp. 135–144. 10.1016/0020-7403(85)90054-2

XXI. Sayles, R. S., T. R. Thomas, and J. Anderson. “Measurement of the Surface Microgeometry of Articular Cartilage.” Journal of Biomechanics, vol. 12, no. 4, 1979, pp. 257–267. 10.1016/0021-9290(79)90068-X

XXII. Stokes, V. K. “Couple Stresses in Fluids.” Physics of Fluids, vol. 9, no. 9, 1966, pp. 1709–1715.

XXIII. Tandon, P. N., et al. “Role of Ultrafiltration of Synovial Fluid in Lubrication of Human Joints.” International Journal of Mechanical Sciences, vol. 27, 1985, pp. 29–37. 10.1016/0020-7403(85)90063-3

XXIV. Tavassoli Kajani, M., M. Ghasemi, and E. Babolian. “Numerical Solution of Linear Integro-Differential Equations Using Sine–Cosine Wavelets.” Applied Mathematics and Computation, vol. 180, no. 2, 2006, pp. 569–579. 10.1016/j.amc.2005.12.044

XXV. Tepei, N. “Lubrication with Micropolar Fluids and Its Application to Short Bearings.” Journal of Tribology, vol. 101, no. 3, 1979, pp. 356–364. 10.1115/1.3453375

XXVI. Torzilli, P. A., and V. C. Mow. “On the Fundamental Fluid Transport Mechanisms through Normal and Pathological Articular Cartilage during Function.” Journal of Biomechanics, vol. 9, no. 9, 1976, pp. 587–606. 10.1016/0021-9290(76)90100-7

XXVII. Tsukamoto, Y., M. Yamamoto, and K. Mabuchi. “Boundary Lubricating Property of Synovial Fluid on Artificial Materials and Lubrication of Artificial Joints.” Journal of the Japanese Orthopaedic Association, vol. 57, no. 1, 1983, pp. 91–99.

XXVIII. Walicka, A. E. “Inertia Effects in Porous Squeeze Film Biobearing with Rough Surfaces Lubricated by a Power-Law Fluid.” Special Topics & Reviews in Porous Media, vol. 3, no. 3, 2012, pp. 247–256.

XXIX. Walicki, E., and A. Walicka. “Inertia and Couple-Stress Effects on Squeeze-Film Characteristics with Reference to Biological Bearings.” TriboTest, vol. 8, no. 3, 2001, pp. 195–203. 10.1002/tt.3020080302

XXX. Wang, Y., T. Yin, and L. Zhu. “Sine–Cosine Wavelet Operational Matrix of Fractional Order Integration and Its Applications.” Applied Mathematics and Computation, vol. 241, 2014, pp. 174–184. 10.1186/s13662-017-1270-7

XXXI. Yousif, A. E., and A. A. Al-allaq. “The Hydrodynamic Squeeze Film Lubrication of the Ankle Joint.” International Journal of Mechanical Engineering and Applications, vol. 1, no. 2, 2013, pp. 34–42. 10.11648 /j.ijmea.20130102.12